catalysts

MDPI

Article

Promoter Effect on Carbon Nanosphere-Encapsulated Fe-Co Catalysts for Converting CO_2 to Light Olefins

Daniel Weber [1,†], Akash Gandotra [1,†], John Schossig [2], Heng Zhang [3], Michael Wildy [2], Wanying Wei [2], Kevin Arizapana [2], Jin Zhong Zhang [3], Ping Lu [2,*] and Cheng Zhang [1,*]

1 Department of Chemistry, Physics and Mathematics, Long Island University (Post), Brookville, NY 11548, USA; daniel.weber4@my.liu.edu (D.W.); akash.gandotra@my.liu.edu (A.G.)
2 Department of Chemistry and Biochemistry, Rowan University, Glassboro, NJ 08028, USA; schoss43@students.rowan.edu (J.S.); wildym28@rowan.edu (M.W.); weiw8@rowan.edu (W.W.); arizap27@students.rowan.edu (K.A.)
3 Department of Chemistry and Biochemistry, University of California, Santa Cruz, CA 95064, USA; hzhan290@ucsc.edu (H.Z.); zhang@ucsc.edu (J.Z.Z.)
* Correspondence: lup@rowan.edu (P.L.); cheng.zhang@liu.edu (C.Z.); Tel.: +1-856-256-5463 (P.L.); +1-516-299-2013 (C.Z.); Fax: +1-516-299-3944 (C.Z.)
† These authors contributed equally to this work.

Abstract: For this work, we investigated the promotor effect (M = Na^+, K^+, Ce^{3+}, Zn^{2+}, Mn^{2+}) on carbon nanosphere-encapsulated bimetallic Fe-Co core–shell catalysts for CO_2 hydrogenation, promising selectivity for converting CO_2 to light olefins. The fresh and spent catalysts were characterized using a combination of experimental techniques such as scanning electron microscopy (SEM), X-ray diffraction (XRD), thermogravimetric analysis and differential scanning calorimetry (TGA–DSC), and Raman spectroscopy, and our results reveal that the addition of the promotor M enhanced the formation of graphitic carbon and metal carbides in the promoted catalysts when compared with the unpromoted catalysts. The metal carbides were determined to be the active sites for the production of light olefins.

Keywords: CO_2 hydrogenation; light olefins; heterogeneous catalysis; carbon nanosphere encapsulated metal; Fe-Co bimetallic; promotor effect

Citation: Weber, D.; Gandotra, A.; Schossig, J.; Zhang, H.; Wildy, M.; Wei, W.; Arizapana, K.; Zhang, J.Z.; Lu, P.; Zhang, C. Promoter Effect on Carbon Nanosphere-Encapsulated Fe-Co Catalysts for Converting CO_2 to Light Olefins. *Catalysts* **2023**, *13*, 1416. https://doi.org/10.3390/catal13111416

Academic Editor: Xiujie Li

Received: 18 September 2023
Revised: 30 October 2023
Accepted: 2 November 2023
Published: 4 November 2023

1. Introduction

Abundant CO_2 emissions have detrimental effects on the environment [1]. Consequently, sea levels are rising, the number of hurricanes and wildfires is growing, and more dangerous heat waves and severe droughts are occurring in many areas. Therefore, there is a pressing need to regulate CO_2 emissions to alleviate their negative impact on the environment. Transforming CO_2 into value-added chemicals and fuels is highly desirable for CO_2 emission mitigation [2,3].

The catalytic conversion of CO_2 into value-added chemicals and fuels is one of the most promising approaches for CO_2 emission mitigation [1,3–16]. Among the methods used for the catalytic conversion of CO_2, a highly favorable route is selective CO_2 hydrogenation to produce value-added chemicals such as light olefins [4,5]. Light olefins (C_2-$C_4^=$) are the building blocks for the production of various polymers and plastics in a wide variety of applications [3,8,17–19]. One primary pathway to produce light olefins from CO_2 conversion by hydrogen (H_2) is the CO_2 Fischer–Tropsch synthesis (CO_2-FTS) route, which consists of two successive processes: the reverse water–gas shift (RWGS) reaction ($CO_2 + H_2 \rightarrow CO + H_2O$, $\Delta H_0^{298} = 41.1$ kJmol^{-1}) and subsequent Fischer–Tropsch synthesis (FTS) ($nCO + 2nH_2 \rightarrow (CH_2)n + nH_2O$, $\Delta H_0^{298} = -210.2$ kJmol^{-1}, $n = 2$) [3,6–12]. Another reaction path is the methanol (MeOH)-mediated route, which consists of two consecutive processes: converting CO_2 to MeOH and a subsequent MeOH-to-olefin conversion

process (MTO) [5,13]. Additionally, there are some reactions, for example, olefin hydrogenation ($(CH_2)_n + H_2 \rightarrow C_nH_{2n+2}$, $\Delta H_0^{298} = -136.3$ kJmol^{-1}, $n = 2$) and CO_2 methanation ($CO_2 + 4H_2 \rightarrow CH_4 + 2H_2O$, $\Delta H_0^{298} = -165.0$ kJmol^{-1}), that can compete with the formation of light olefins. The complex reaction network and thermodynamics involved in CO_2 hydrogenation indicates that it is challenging to develop catalysts for a one-step process to selectively produce light olefins.

Other catalytic processes for CO_2 valorization, such as methanol synthesis (proposed by Cordero-Lanzac et al. [14]) and dimethyl ether (DME) synthesis (proposed by Ateka et al. [15,16]) have been widely studied, but they are not the focus of this work.

Different catalysts based on transition metals or metal carbides have been extensively studied for CO_2 conversion [10,11,17,20,21]. To improve catalyst performance, it is desirable to prepare stable small metal particles under reaction conditions. Confined nanocatalysts based on "nanoreactors" have received growing attention [22–35]. One of the promising approaches is to construct core–shell catalysts wherein the core serves as the nanoreactor, the metal species within the core acts as the active sites, and the shell acts as the boundary to hold the metal species in the core to prevent from metal agglomeration. In particular, core–shell nanocatalysts have been studied extensively [22,23,26,35–47]. Gupta et al. designed a core–shell nanoreactor with partially graphitized carbon in the shell and Fe_3O_4 and Fe_5C_2 in the core for CO_2 hydrogenation [38]. Fe_3O_4 nanoparticles encapsulated within graphitic carbon shells are more efficient than conventional catalysts [43,44]. Porous graphene-confined Fe-K and carbon-confined magnesium hydride nanolamellae are highly efficient catalysts for the direct hydrogenation of CO_2 to light olefins [48,49]. Fe_3O_4 was found to be responsible for RWGS, with the metallic Fe and iron carbides activating CO to generate hydrocarbons [50]. Previous works in our lab have involved synthesizing carbon nanosphere-encapsulated Fe and Fe-Co core–shell catalysts and evaluating their utility for CO_2 hydrogenation [51,52]. The graphitic carbon with defects in the shell and a mixture of metal oxides, metallic metal, and metal carbides in the core was evidenced by SEM, TEM, XRD, and XPS [51]. The Fe_3O_4@carbon nanostructured catalyst enjoys the benefit of the effective diffusion of carbon atoms from the shell into the core to form a Fe_5C_2 carbide phase that is active for hydrogenation [40,43].

Despite being widely studied in the context of CO_2 hydrogenation, Fe-based catalysts usually have low selectivity toward light olefins. The use of suitable metals/promotors to boost the yield of light olefins by adjusting electronic and structural properties has been extensively studied [53–65]. Doping the catalyst with a second metal may improve the yield of light olefins by forming a highly active interface. Xu et al. studied the role of Fe-Co interaction in ternary $ZnCo_{0.5}Fe_{1.5}O_4$ catalysts and found that during the CO_2 hydrogenation, Fe atoms in the Fe-Co alloy enhances the generation of active sites for production of light olefins [53]. Alkali metals have often been used as promotors to modulate electronic properties [54–60], while metals such as Mn, Ce, and Ca have been utilized as structural promotors [61–63]. Transition metals (e.g., Zn, Co, Cu, V, and Zr) have been used as both electronic and structural promotors [56]. When modified with alkali promoters, Fe-based catalysts demonstrate higher olefin selectivity due to an increase in the adsorption of CO_2 on the Fe phases and consequently suppress H_2 chemisorption, which inhibits olefin readsorption to form alkanes, leading to higher olefin yields [60,64,65]. Our previous study described the conversion of CO_2 to light olefins with favorable catalytic activity through using a carbon nanosphere (CNS)-encapsulated bimetallic Fe-Co catalyst [52].

In this work, we introduce promotors M (M = Na, K, Ce, Mn, Ce, and Zn), which have been studied widely, to the core of CNS-encapsulated bimetallic Fe-Co catalysts to modify the metal species to further improve the catalytic activity of the catalysts for the hydrogenation of CO_2 to light olefins. The promoted M-CNS-FeCo catalysts were synthesized using a diffusion impregnation method, and about 1 wt% of M was determined using ICP-MS analysis. The synthesized catalysts were evaluated for CO_2 hydrogenation at atmospheric pressure, and testing results revealed that the addition of a promotor boosted the production of light olefins. SEM analysis, XRD analysis, TGA-DSC, and Raman

spectroscopy were utilized to characterize the fresh and spent catalysts. Our results revealed that the addition of the promotor M enhanced the formation of graphitic carbon and metal carbides in the promoted catalysts when compared with the unpromoted catalysts. The metal carbides were determined to be the active sites for the production of light olefins.

2. Results and Discussion

2.1. Diffusion Process Used to Synthesize Promoted M-CNS-FeCo (M = Ce, Na, K, Mn, Zn)

Several means were utilized to introduce the promotor to the catalysts [49,55–57,59,61–65]. Among them, the most widely used approach is wetness impregnation method [57,59,61,62,64]. However, this method was mainly used to decorate the surface of the catalysts. For the present work, we attempted to introduce the promotor M to the core of CNS to modify the bimetallic Fe-Co. The process used to prepare the promoted M-CNS-FeCo (M = Ce, Na, K, Mn, Zn) is illustrated in Scheme 1. Firstly, the prepared CNS-FeCo was mixed with saturated M salt solution and subjected to an ultrasound for 30 min to expediate the diffusion of the M salts to the core of the CNS. Secondly, we used rotovap to evaporate the solvent. During the rotary evaporation process, uniform rolling assisted the diffusion and simultaneously impregnated the promotor salts on the surface of the CNS; the last step was to remove the M salts on the surface of the CNS using a sufficient amount of Di-H_2O. Metal contents for Fe, Co, and M wt% in M-CNS-FeCo were determined, and the results are shown in Table 1. Sufficient experiments were conducted to investigate the effect of the ultrasound duration, rotavap duration, water amount usage, and rinsing duration on promotor content and catalytic performance. Initially, approximately 5 wt% promoted catalysts were prepared after the series of the experiments carried out via in the above steps. The surface promotors could be washed off easily. Some of the promotors in the core could have been leached out too, but we were able to control the rinsing process to maintain approximately 1 wt% of M content in each individual promoted M-CNS-FeCo through using this synthetic approach. The consistency of the M metal content in the promoted samples indicated the validity of this synthetic process.

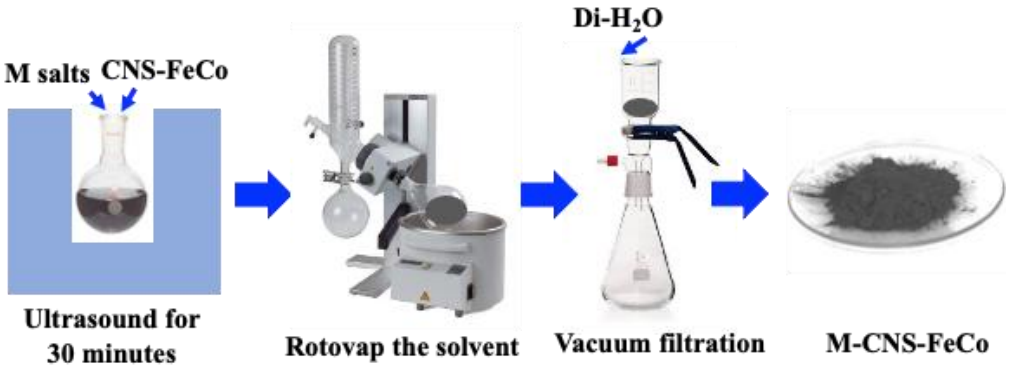

Scheme 1. Illustration of synthesis of promoted M-CNS-FeCo catalysts.

Table 1. Metal contents (%) in M-CNS-FeCo catalysts.

Catalysts	Fe (wt%)	Co (wt%)	M (wt%)
CNS-FeCo	6.38 ± 0.11	15.23 ± 0.17	none
Ce-CNS-FeCo	6.38 ± 0.11	15.23 ± 0.17	Ce: 0.96 ± 0.05
Na-CNS-FeCo	6.38 ± 0.11	15.23 ± 0.17	Na: 0.94 ± 0.05
K-CNS-FeCo	6.38 ± 0.11	15.23 ± 0.17	K: 1.02 ± 0.07
Mn-CNS-FeCo	6.38 ± 0.11	15.23 ± 0.17	Mn: 1.05 ± 0.07
Zn-CNS-FeCo	6.38 ± 0.11	15.23 ± 0.17	Zn: 0.98 ± 0.05

2.2. Catalytic Performance of Promoted M-CNS-FeCo (M = Ce, Na, K, Mn, Zn)

The above-mentioned synthesized catalysts were evaluated for CO_2 hydrogenation under identical testing conditions to facilitate a direct comparison with the unpromoted CNS-FeCo. Figure 1a–e depict catalytic performance (hydrocarbon distribution, CO_2 conversion, CO selectivity) as a function of temperature over promoted catalysts (Figure 1a–e: Ce, K, Mn, Na, Zn, respectively) to facilitate a comparison with the unpromoted catalyst (Figure 1f). It was demonstrated that the addition of promotor M (M = Ce, K, Mn, Na, Zn) to CNS-FeCo enhanced the catalytic performance in terms of light olefins in the hydrocarbon distribution for CO_2 hydrogenation at different temperatures when compared with the unpromoted catalysts. As the temperature increased from 275 to 400 °C, the CO_2 conversion generally increased for all catalysts; the CO selectivity increased from 275 to 350 °C but dropped at 400 °C. Regarding the hydrocarbon distribution, the hydrocarbon contained CH_4, light olefins (C_2-$C_4^=$), light alkanes (C_2-$C_4^{(0)}$, and C_{5+} ($C_{5+}^=$, C_{5+}^0, $C_{6+}^=$, C_{6+}^0, $C_{7+}^=$, C_{7+}^0); the main product in all catalysts (promoted and unpromoted) was CH_4, and it decreased as temperature increased from 275 to 350 °C and then backed up for most catalysts, while it continued to drop for the Mn-promoted catalysts. For the unprompted catalyst, almost no light olefins were produced at temperatures lower than 275 °C, but the addition of a promotor enabled light olefin production even at 275 °C. As the temperature increased from 275 to 350 °C, the amount of light olefins produced increased and peaked at 350 °C before starting to drop for most catalysts, except for the Mn-promoted catalyst, which continued to rise at 400 °C. Lower temperatures (275~325 °C) were conducive to light alkane production, especially for the Na- and K-promoted catalysts. Almost no long chains of C_{5+} hydrocarbons were produced for all catalysts.

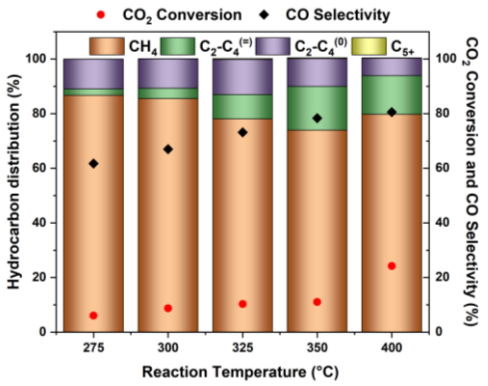

(**a**) Ce

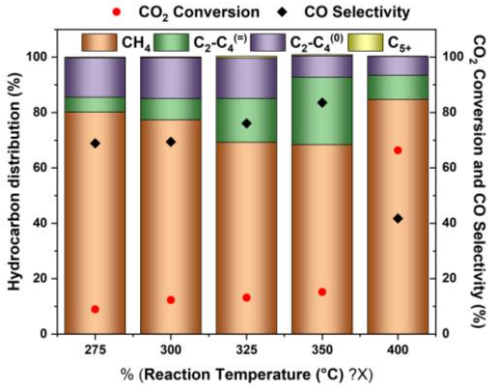

(**b**) K

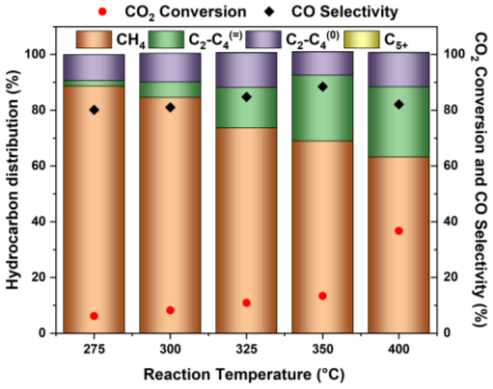

(**c**) Mn

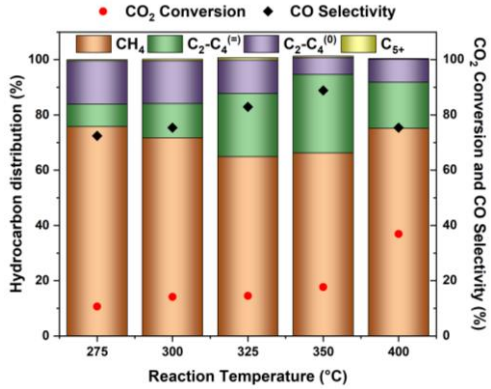

(**d**) Na

Figure 1. *Cont.*

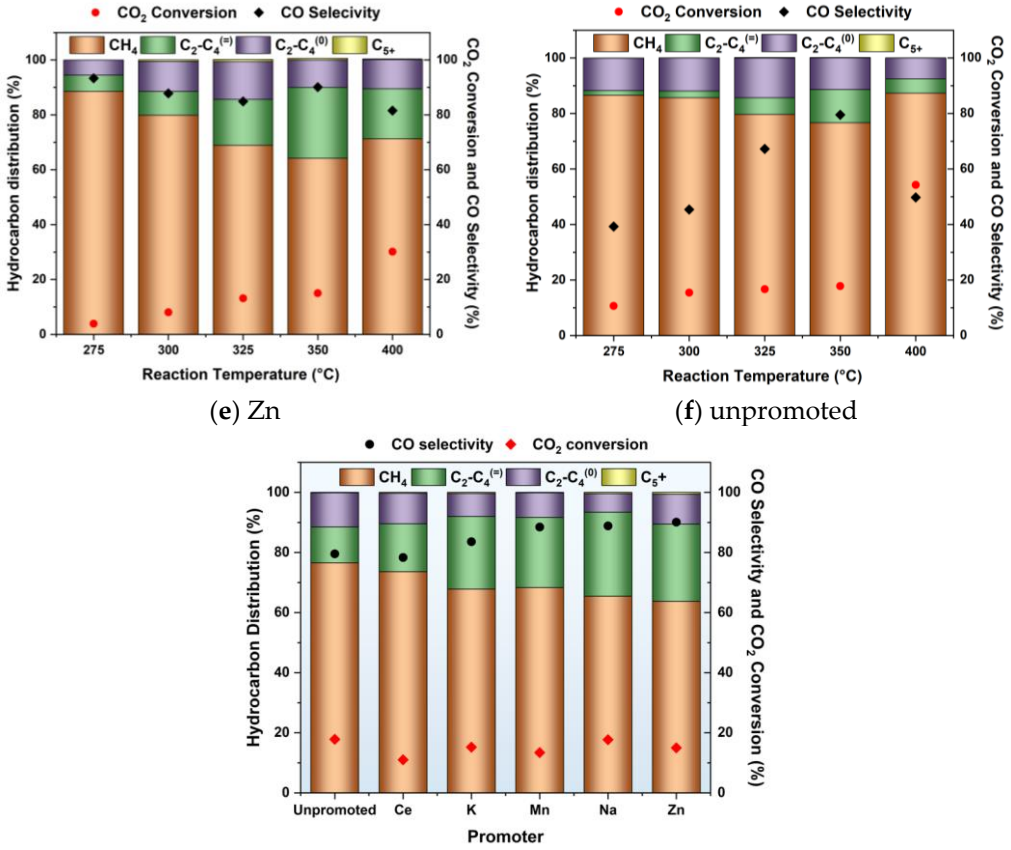

Figure 1. CO_2 hydrogenation catalytic performance (CO_2 conversion, CO selectivity, and hydrocarbon distribution) as a function of temperature over promoted M-CNS-FeCo to compare with unpromoted catalysts: (**a**) Ce; (**b**) K; (**c**) Mn; (**d**) Na; (**e**) Zn; (**f**) unpromoted; (**g**) catalytic performance as a function of promotors. Testing conditions for (**a**–**f**): catalyst, 0.1 g; GHSV: 24,000 mL g^{-1}·h^{-1}; Temperature: 275~400 °C; H_2/CO_2 = 3:1; P: atmospheric pressure. The testing conditions for (**g**) were the same, except the temperature was kept at 350 °C.

The catalytic performance data of hydrocarbon distribution, CO_2 conversion, and CO selectivity at 350 °C for various promoted catalysts are summarized in Figure 1g; the promotor effect could easily be perceived for the production of light olefins among the promoted and unpromoted catalysts, with Na being the most promising promoter, enhancing the production of light olefins at 350 °C.

As shown in Figure 1b,d, the catalytic performance trends for the Na- and K-promoted catalysts were similar. Alkali metals such as K and Na, as electron donors, seemingly adjusted the electronic properties of the Fe/Co sites in the core of the CNS, which facilitated the production of light olefines and inhibited secondary hydrogenation to light alkanes at 350 °C. The Mn, Ce metals, as structural promotors, decorated the structural properties of the Fe/Co sites in the core of CNS, which promoted the production of light olefins at higher temperatures (>350 °C) (Figure 1a,c). The transition metal Zn, as both an electronic and structural promotor, behaved slightly differently from the other promoted catalysts in terms of the trends for CO selectivity as the temperature changed.

A previous work showed that the CO_2 conversion can be significantly enhanced with the introduction of Co into the Fe catalyst [52]. The intimate contact between the Fe and Co sites favored the production of C_2-$C_4^=$. Xu et al. investigated the roles of Fe-Co interactions over ternary $ZnCo_{0.5}Fe_{1.5}O_4$ catalysts and unveiled that during CO_2 hydrogenation, the formation of electron-rich Fe atoms in the Fe-Co alloy phase significantly boosted the generation of active metal carbides phases [53]. Similarly, Chaipraditgul et al. found

that the addition of the transition metal Co to Fe-based catalysts remarkably altered the interaction between the adsorptive CO_2 and H_2 and the surfaces of the metal catalysts [64].

With the addition of a promotor, the surface of the metal species became carbon-rich and hydrogen-poor, which facilitated C−C coupling and therefore the formation of light olefins and the suppression of CH_4, as illustrated in Figure 1. Among the promotors investigated, it was found that the Na and K performed similarly with respect to enhancing the catalytic performance in terms of light olefin selectivity and CO_2 conversion. Adding alkali metals (i.e., Na, K) could enhance CO_2 adsorption on the more electron-rich Fe/Co phases, facilitate the generation of active sites χ-$(Fe_{1-x}Co_x)_5C_2$, and suppress H_2 chemisorption, which inhibits olefin re-adsorption for secondary hydrogenation to alkanes [56–58,63,66]. As evidenced in Figure 1, the Mn-promoted catalysts performed slightly different from other promoted catalysts. The addition of Mn to the Fe-Co species in the core of the CNS might have allowed for an increase in the catalyst's basicity, which prevented the secondary hydrogenation of olefins into paraffins. Furthermore, the synergistic effects between Fe-Co and Mn could promote the production of Fe carbides and improve CO_2 dissociation and the conversion of CO_2 to hydrocarbons. Additionally, the addition of Mn could reduce the amount of weakly adsorbed H atoms and consequently lessen the hydrogenation aptitude, which could explain why the Mn-promoted CNS-FeCo catalyst had a higher level of light olefin production even at a higher temperature (400 °C) when compared with the other promoted and unpromoted CNS-FeCo catalysts. Similar effects were observed by Liang et al. and Jiang et al. [61,62]. Ce, as a structural promoter, can restrain the growth of an Fe_2O_3 crystallite, weaken the interaction between Fe and cobalt, and enable and ease the reduction of iron oxide and cobalt oxides, as confirmed by the studies conducted by Zhang et al. [63]. Conversely, the addition of Zn can adjust the basicity of the Fe-Co surface, increase the number of active sites for the adsorption of CO_2 and H_2, and ease the reducibility of metal oxides to a certain degree, as confirmed by Witoon et al.'s work [67].

In summary, the final products produced from the process are CO, CH_4, light olefins (C_2-$C_4^=$), light alkanes (C_2-$C_4^{(0)}$, and trace amounts of C_{5+} ($C_{5+}^=$, C_{5+}^0, $C_{6+}^=$, C_{6+}^0, $C_{7+}^=$, C_{7+}^0); the introduction of promotors such as Na, K, Mn, Ce, and Zn to the core of the CNS-FeCo catalysts boosted the production of light olefins for CO_2 hydrogenation.

2.3. Physicochemical Properties of Promoted M-CNS-FeCo (M = Ce, Na, K, Mn, Zn)

The Na-promoted catalysts were selected to investigate the morphology of the catalysts before and after CO_2 hydrogenation. Figure 2a,b display the SEM images of the fresh Na-promoted catalyst before CO_2 hydrogenation, and Figure 2c,d exhibit the SEM images of the spent Na-promoted catalysts after CO_2 hydrogenation. More agglomerations were observed for the spent catalysts, which confirmed the deactivation of the catalysts over the time of the stream.

Figure 3 shows the XRD patterns of the fresh and spent M-CNS-FeCo catalysts with different promoters (i.e., Na, K, Ce, Mn, and Zn) at 2θ = 10.0–70.0°. The patterns could be attributed to a mixture of carbon, metal oxides, metal carbides, and metallic metals, as denoted in our XRD analysis. The broad peaks in the 10.0–20.0° range are characteristic of amorphous carbon, indicating the presence of amorphous carbon (defects) on the CNS. The intensity of these broad peaks were increased for the Na- and K-promoted catalysts, indicating a relative higher amount of amorphous carbon when compared to the Ce-, Mn- and Zn- promoted catalysts. The peak at 2θ = 26.0° was indexed to the (002) plane of graphite (PDF 00-41-1487) [68]. The intensity of this graphite carbon peak enhanced after the addition of the M promotors (M = Ce, K, Mn, Na, Zn), indicating that the M promotors might have facilitated the conversion of the amorphous carbon into graphitic carbon. The diffraction peaks at 2θ = 18.5, 30.4, 35.8, and 53.8° correspond to the (111), (220), (311), and (422) crystal facets of Fe_2O_3-Co_2O_3, respectively (PDF 00-039-1346). The peaks at 2θ = 30.2, 35.5, 57.3, and 63.0° were assigned to the (220), (311), (511), and (440) facets of Fe_3O_4-Co_3O_4, respectively (PDF 00-065-0731). The peak at 2θ = 42.7° could be attributed to the (110) plane of metallic Fe-Co (PDF 00-006-0696), while the 45.5° peak

could be attributed to the (112) plane of Fe_5C_2-Co_5C_2 (PDF 00-051-0997). In the spent M-CNS-FeCo, the broad amorphous carbon peak in the range of 10.0–20.0° increased for the Zn-and Ce-promoted catalysts, suggesting more carbon deposition on the catalysts. Interestingly, the peaks for Fe_2O_3-Co_2O_3, Fe_3O_4-Co_3O_4, and the metallic metals Fe-Co almost disappeared for the spent catalysts. On the contrary, the peak for the iron–cobalt carbide Fe_5C_2-Co_5C_2 at 45.5° drastically increased, which indicated that the metal carbides were the active sites for CO_2 hydrogenation. The carbonaceous intermediates possibly further carbonized bimetallic Fe-Co, forming the Fe-Co metal carbide phase, as evidenced by the nearly complete disappearance of metal oxides. Our XRD data confirmed that the iron–cobalt species (mainly iron–cobalt carbides) encapsulated in CNS are in a more reduced state. The reduction of metal oxides and the dominant form of metal carbides in the spent catalyst resembled a favorable environment for CO_2 hydrogenation, as evidenced by the catalytic performance. Compared to the unpromoted catalysts, it seemed that the M promotors played a pivotal role in promoting metal carbide formation within the core of CNS during CO_2 hydrogenation. The exception to this are the Zn-promoted catalysts, which retained metal oxide species. The presence of oxide phases weakened the conversion of CO_2, as confirmed by the catalytic performance (Figure 1e).

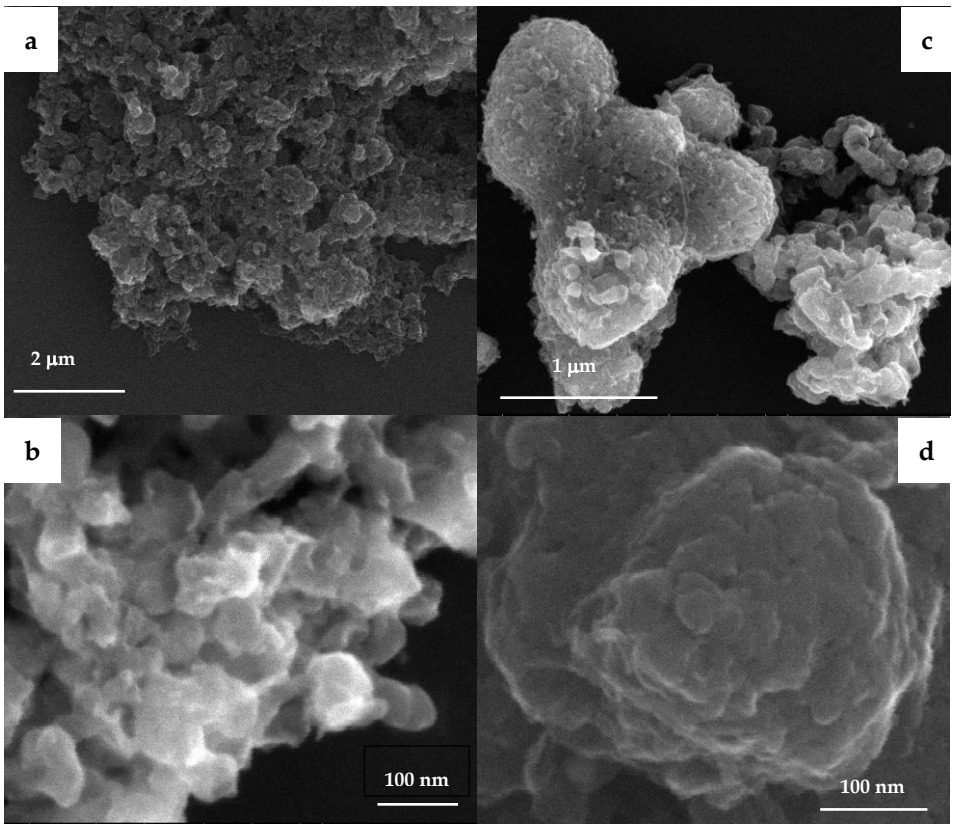

Figure 2. SEM images of fresh Na-CNS-FeCo catalyst before CO_2 hydrogenation (**a**,**b**) and spent Na-CNS-FeCo catalyst after CO_2 hydrogenation (**c**,**d**).

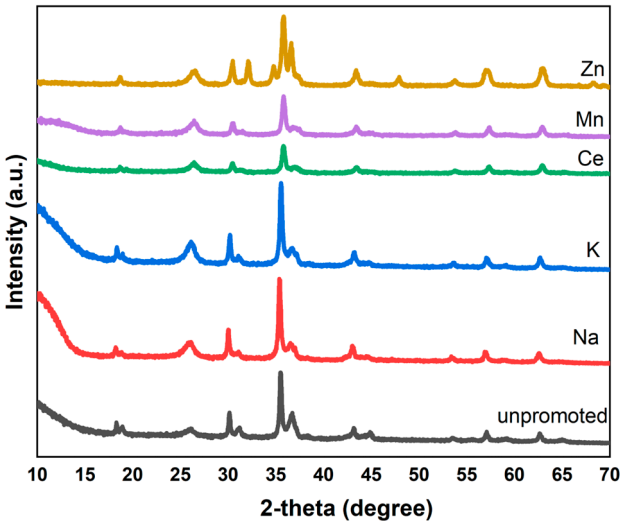

(**a**)

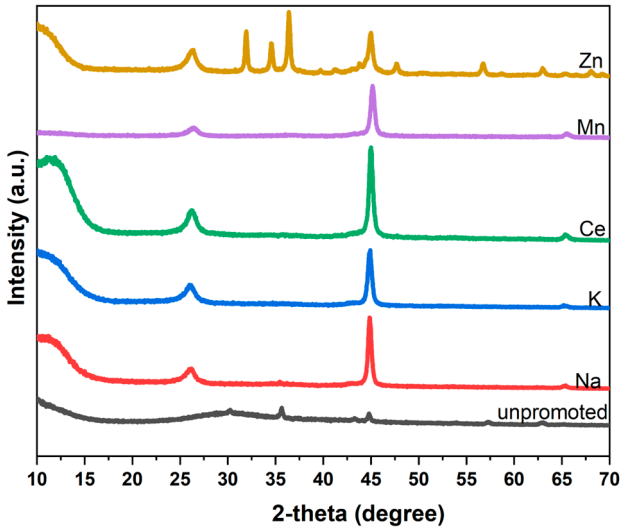

(**b**)

Figure 3. XRD for (**a**) fresh M-CNS-Fe_1Co_2 catalyst before CO_2 hydrogenation and (**b**) spent M-CNS-Fe_1Co_2 catalyst after CO_2 hydrogenation.

Raman spectra of the fresh and spent promoted M-CNS-FeCo catalysts and the unpromoted catalyst CNS-FeCo are shown in Figure 4. The peaks at 1358 cm^{-1} correspond to the D-band associated with defects and edge planes. The presence of a strong D band indicates a high density of defects and porosity that could be important for reactant molecules to access the active sites in the core [51,52]. The peaks at 1585 cm^{-1} (G-band) were ascribed to the in-plane vibrations of the E_{2g} graphene sheet zone-center mode [69], while the peaks at 2700 cm^{-1} (G′-band) were attributed to the stacking order of graphene layers [70]. Comparing the fresh promoted and unpromoted catalysts (Figure 4a), the fresh promoted catalysts contained higher amounts of graphitic carbon in the G band and G′ band relative to the amount of amorphous carbon in the D band, indicating that the promotor M facilitated the formation of graphitic carbon, consistent with the XRD data (Figure 3a). Comparing the fresh and spent promoted catalysts, as shown in Figure 4b, there was a significant increase in the intensity of the amorphous carbon (D band) relative to the graphitic carbon (G band) for the spent catalysts, indicating that carbon deposition occurred after CO_2 hydrogenation, and this was also confirmed by the XRD data (Figure 3b). The high content

of graphitic carbon was consistent with the graphitic shell in the CNS, as reported in an earlier work [51].

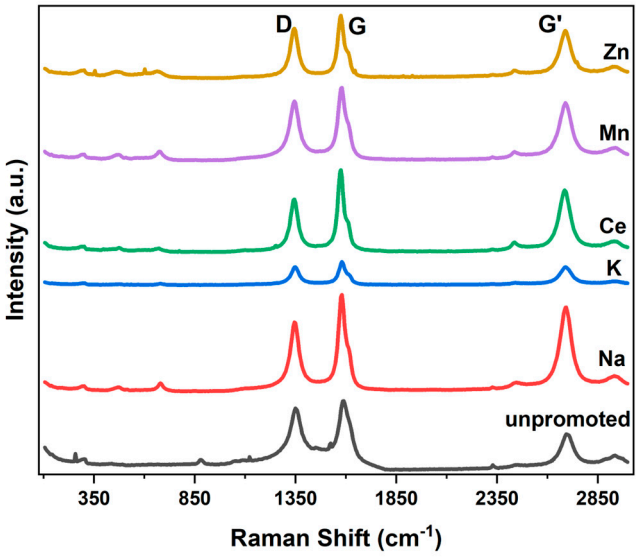

(**a**)

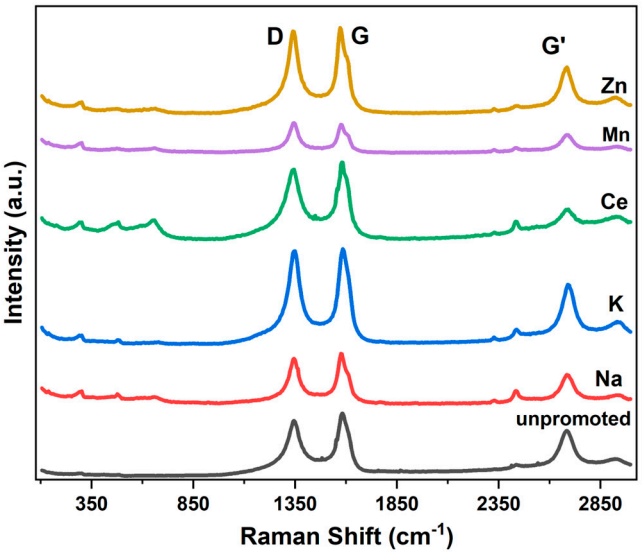

(**b**)

Figure 4. Raman spectra of (**a**) fresh catalysts and (**b**) spent catalysts.

Figure 5 shows the TGA–DSC results of both the fresh and spent M-promoted catalysts. Figure 5a delineates the degradation profiles of the fresh M-promoted catalysts. Both samples displayed minimal mass variation below 650 °C, possibly attributable to thermal stable graphitic carbon, with a meager 2.5% change for all fresh catalysts. An exothermic peak was observed at around 530~560 °C for all spent catalysts, indicating that a chemical reaction involving the amorphous carbon burning occurred, with an overall weight loss of 7%. The higher amount of amorphous carbon for the spent catalysts compared to the fresh catalysts was due to the carbon deposition during CO_2 hydrogenation, which is consistent with the XRD and Raman data, and reflected the deactivation of the catalyst due to the carbon deposition over the time of the stream. Overall, the TGA data demonstrated the thermal-stable nature of the CNS-encapsulated Fe-Co catalysts.

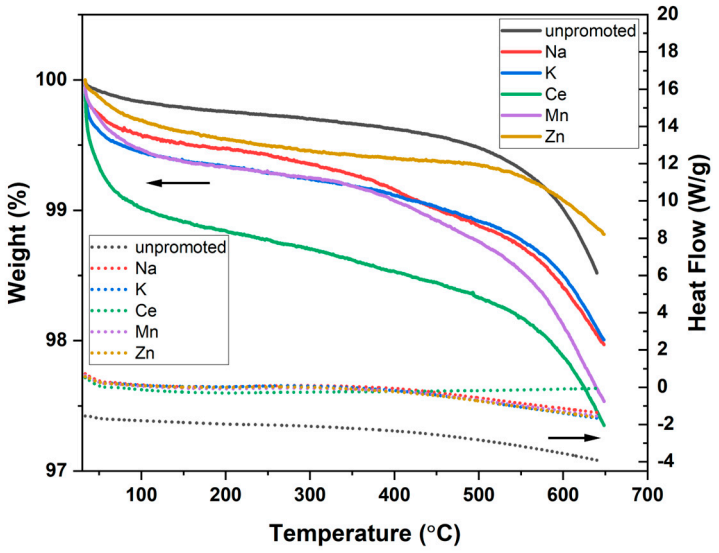

(**a**)

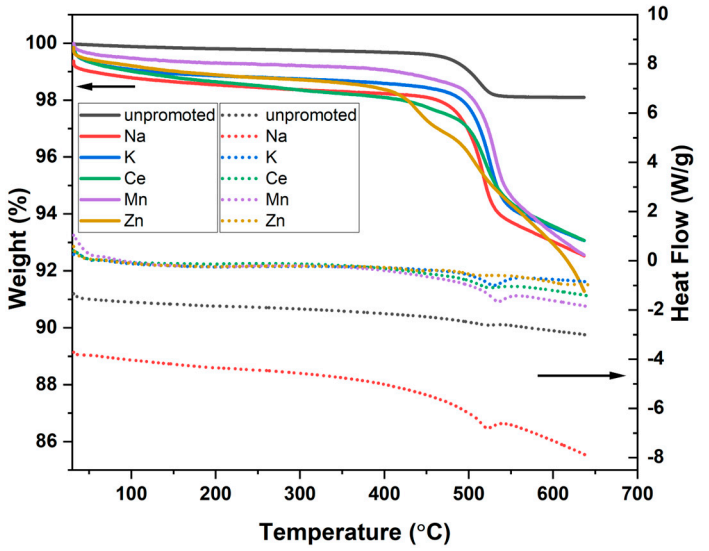

(**b**)

Figure 5. TGA–DSC of (**a**) fresh and (**b**) spent M–CNS–FeCo catalysts.

2.4. Mechanistic Insights of Promoted M-CNS-FeCo for CO_2 Hydrogenation

For comparison, CNS with an empty core (metal species were completely removed from the core), a promotor diffused into the CNS with an empty core, and a promotor impregnated onto the surface of the CNS with empty core were evaluated and showed no catalytic activity for CO_2 hydrogenation, as illustrated in Scheme 2. The catalytic activity for CO_2 hydrogenation was observed only when a CNS-encapsulated metal species, such as Fe or Fe-Co, was added [51,52]. In addition, other controlled catalysts were prepared using the incipient wetness method to introduce the promotors on the surface (shell) of CNS-FeCo; the resulting catalysts performed much worse than the unpromoted CNS-FeCo catalyst for the hydrogenation of CO_2 to light olefins. Therefore, the effect of the presence of the promoter component in the carbon shell or the residue promoter in the carbon shell on the catalytic performance of promoted CNS-FeCo catalysts in the hydrogenation of CO_2 could be neglected. The catalytic performance was boosted only after the promotor ions were diffused into the core of CNS to make contact with Fe-Co. These controlled

experiments indicated that the metal in the core is essential and that the diffusion of the promotor into the metal core is critical to adjust the electrical and structural properties of the metals. Therefore, it is important to have three components in the catalytic composition for CO_2 hydrogenation: CNS in the shell, encapsulated Fe-Co in the core, and a promotor. CNS acted as the carbon source and confined reactor, Fe-Co served as the active sites in the core, and the promotor functioned as a booster to improve the production of light olefins (Scheme 2). As evidenced by the XRD analysis, Raman spectroscopy, and TGA results, the M promotor facilitated the formation of graphitic carbon and metal carbides.

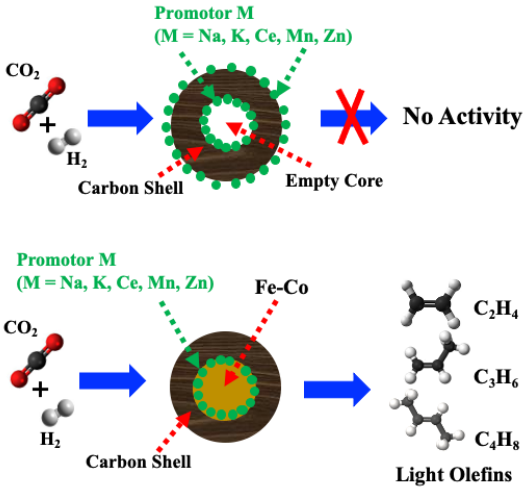

Scheme 2. Illustration of CO_2 hydrogenation over promoted M-CNS–empty core and promoted M-CNS-FeCo catalysts.

Based on the product distribution (CO, CH_4, $C_2-C_4^{(=)}$, $C_2-C_4^{(0)}$, C_{5+}), the reaction pathway over the catalyst M-CNS-FeCo follows the CO_2-FTS route, which consists of two successive processes: the reverse water–gas shift (RWGS) reaction ($CO_2 + H_2 \rightarrow CO + H_2O$) and subsequent Fischer–Tropsch synthesis (FTS) ($nCO + 2nH_2 \rightarrow (CH_2)n + nH_2O$). As suggested previously [51], the mechanisms of light olefin synthesis by CO_2 hydrogenation involved C−O bond cleavage and C−C bond formation [36,51]. Through the CO_2-FTS process over the promoted M-CNS-Fe_1Co_2 catalysts, the Fe_2O_3/Co_2O_3 phase was reduced by hydrogen to Fe_3O_4-Co_3O_4 as the active phase for the RWGS reaction, which was then reduced to Fe-Co in metallic states and further carbonized to form metal carbides, as confirmed by our XRD analysis. The reactant gases CO_2 and H_2 diffused through the porous carbon shell into the core and reacted with Fe_3O_4-Co_3O_4 to form carboxylate species (*CO_2, *representing the adsorbed state) after CO_2 was absorbed and stimulated on the active phases of Fe_3O_4-Co_3O_4 for RWGS. The adsorbed H then hydrogenated the resulting *CO_2 to form an *HOCO intermediate that then dissociated into *CO and *OH, with *CO subsequently dissociating into *O and *C. The produced *C could diffuse into the metal Fe-Co to form Fe-Co carbides, the active phase for the Fisher-Tropsh synthesis reaction as confirmed by the XRD studies performed for this work. The C* on the surface of the metal carbides was then hydrogenated to CH_x* species. CH_x* + CH_x* and C* + CH_x* are the most likely reaction pathways for C−C coupling [5,71].

Some earlier works shed light on how the promoters affected the behavior of the iron-based catalysts [55,56]. Yang et al. uncovered that, in their study, the addition of promoters altered the equilibrium between the iron oxides and iron carbides in the catalyst, which affected the CO_2 conversion, facilitated the production of C_{2+} olefins, and inhibited the competitive methanation reaction [56]. Similarly, a previous study found that the addition of a Na promoter into Fe-based catalysts boosted the adsorption of CO_2, enhanced the stability of the active Fe_5C_2 phase, and suppressed the secondary hydrogenation of alkenes [55]. Catalyst regenerability and the removal of coke comprise elements of our ongoing research and will be discussed in future work.

3. Materials and Methods

3.1. Materials

Citric acid was obtained from Acros Organics. Iron powder (200 mesh) and cobalt powder (200 mesh) were purchased from Alfa Aesar. Ammonium hydroxide (28% in water), resorcinol and formaldehyde (37% in water), KNO_3 (99%), $NaNO_3$ (>99%), $Zn(NO_3)_2{\cdot}6H_2O$ (98%), $Ce(NO_3)_3{\cdot}6H_2O$ (99%), and $Mn(NO_3)_2{\cdot}4H_2O$ (>99%) were purchased from Sigma-Aldrich, Saint Louis, MO, USA.

3.2. Synthesis of Promoted M-CNS-FeCo (M = Ce, Na, K, Mn, Zn)

The synthesis of promoted M-CNS-FeCo (M = Ce, Na, K, Mn, Zn) catalysts mainly involved two steps: the first step was to synthesize the CNS–encapsulated Fe−Co catalyst (CNS-FeCo), and the second step was to use a diffusion procedure to impregnate promotors M (Ce, Na, K, Mn, Zn) to CNS-FeCo.

(1) Synthesis of CNS-FeCo

A CNS-encapsulated bimetallic Fe−Co catalyst (CNS-FeCo) was synthesized following a modified previously reported method [36,51,52,71–75]. Specifically, the synthesis of CNS-FeCo involved three steps: The first step was the synthesis of iron polymeric complex solution (0.20 M) and cobalt polymeric complex solution (0.10 M). A total of 0.20 M of iron polymeric complex solution was prepared by adding 19.21 g of citric acid, 5.58 g of iron powder, and 100 mL of de-ionized water to a 500 mL beaker. The above-mentioned mixture was forcefully agitated in air for 48 h, resulting in a clear greenish solution. A total of 0.10 M of cobalt polymeric complex solution was prepared in a similar manner. The second step was polymerization. For this step, 12.20 g of resorcinol, 18.0 g of formaldehyde (37% in water), and 100 mL of 0.20 M of the earlier-prepared iron solution and 40 mL of 0.10 M of the earlier-prepared cobalt solutions were added to a 500 mL round-bottom three-neck flask. The resulting mixture was agitated until resorcinol was dissolved, followed by adding ammonium hydroxide (28% in water) dropwise. The final pH of the mixture reached 10. The resulting slurry was then aged at 85 °C for three hours, with the resulting solid being collected via vacuum filtration and dried at 65 °C in a vacuum oven overnight. The third step was carbonization. For this step, the collected polymer was heated at 85 °C for two hours to remove moisture and then 850 °C for 5 h. The resulting sample is referred to as CNS-FeCo in this study.

(2) Synthesis of M-CNS-FeCo (M = Ce, Na, K, Mn, Zn)

Diffusion was utilized to impregnate promotors to CNS−FeCo. For this, in a 100 mL round-bottom flask, 1.0 g of the earlier-carbonized product was added to metal salts 4.0 g of KNO_3, 3.4 g of $NaNO_3$, 11.9 g of $Zn(NO_3)_2{\cdot}6H_2O$, 17.4 g of $Ce(NO_3)_3{\cdot}6H_2O$, and 10.0 g of $Mn(NO_3)_2{\cdot}4H_2O$ in 20 mL of water, respectively. The resulting mixture was subjected to an ultrasound for 30 min to allow the metal salts to diffuse into the core of the CNS. The vessel was then loaded onto the Buchi® Rotavapor® R-3 evaporator (New Castle, DE, USA) to evaporate at 60 °C until visibly dry. The product was washed with an ample amount of deionized water to remove the metal salts attached to the surface of the CNS. The resulting solid was dried and calcined at 350 °C for five hours. The calcined samples were then grounded into a powder and pelleted to a 40–60 mesh size prior to catalyst testing.

3.3. Catalyst Evaluation

The synthesized catalysts were tested using a standard procedure reported in a previously published work [48]. Further details on the testing procedure and calculation equations are provided in the Supplementary Materials.

3.4. Catalyst Characterization

Metal analyses for Fe, Co were carried out in a manner that has been described in detail previously [51]. Metal analyses for K, Na, Mn, Ce, and Zn were carried out in a

similar manner. A more detailed description of the relevant procedures is provided in the Supplementary Materials.

For SEM and STEM characterization, 1 mg CNS samples were dispersed in 15 mL isopropanol and subjected to an ultrasound for 15 min before measurement. All the solutions were further dropped onto a hexagonal 400-mesh copper grid with a carbon support film with a standard thickness of 3–4 nm (CF400H-Cu-UL, Electron Microscopy Sciences, Hatfield, PA, USA) and allowed to dry in an ambient environment. The samples were imaged using an FEI Quanta 3D Dual Beam SEM operating at 5 kV and 6.7 pA.

The powder XRD, TGA–DSC, and Raman measurements taken for this work were carried out using a method that has been described in detail previously [53] and are provided in the Supplementary Materials.

4. Conclusions

For this work, we synthesized promoted M-CNS-FeCo (M = Na, K, Ce, Mn, Zn) catalysts using a diffusion impregnation method to investigate the promotor effect on carbon nanosphere-encapsulated Fe-Co catalysts for CO_2 hydrogenation. The results from our catalyst tests show that the addition of the M promotor significantly boosted light olefin production, especially for the Na^+-promoted CNS-Fe-Co catalysts. The catalysts were characterized by XRD analysis, Raman spectroscopy, TGA–DSC, and SEM analysis to establish the relationship between their activity and properties. The XRD, Raman, and TGA–DSC data evidenced that the addition of the promotor M boosted the formation of graphitic carbon and metal carbides in the promoted catalysts when compared to the unpromoted catalysts. The metal carbides were the active site for the production of light olefins. The present findings provide a significant insight into the role of promoters in CNS-encapsulated metal catalysts for the conversion of CO_2 into light olefins.

Supplementary Materials: The following supporting information can be downloaded at: https://www.mdpi.com/article/10.3390/catal13111416/s1. Catalyst testing procedure, metal analysis methodology, power XRD, TGA-DSC, and Raman sample preparation and measurements.

Author Contributions: Conceptualization, C.Z.; methodology, C.Z.; software, C.Z.; validation, C.Z., P.L. and J.Z.Z.; formal analysis, D.W., A.G., J.S., H.Z., K.A., W.W. and M.W.; writing—original draft, C.Z.; writing—review and editing, C.Z., P.L. and J.Z.Z.; funding acquisition, C.Z. and P.L.; resources, C.Z.; supervision, C.Z., P.L. and J.Z.Z.; project administration, C.Z. All authors have read and agreed to the published version of the manuscript.

Funding: This work was supported by the National Science Foundation under Grant No. 1955521, 2247399, 2116353, and 2018320. This research was funded by the Startup Fund and the Catalyst Fund from Rowan University, and the Research Grant (#PC 20-22) from the New Jersey Health Foundation.

Data Availability Statement: The data presented in this study are available from the corresponding authors (C.Z. and P.L.) upon request. The data are not publicly available due to privacy reasons.

Acknowledgments: The authors are grateful for the support they received from the U.S. Department of Energy, Office of Science, and Office of Workforce Development for Teachers and Scientists (WDTS) under the Science Undergraduate Laboratory Internships Program (SULI) and Visiting Faculty Program (VFP). We acknowledge Tom Yuzvinsky for providing assistance with electron microscopy and the W.M. Keck Center for Nanoscale Optofluidics for allowing us to use the FEI Quanta 3D Dual beam microscope in UC Santa Cruz.

Conflicts of Interest: The authors declare no conflict of interest.

References

1. Zhang, X.; Zhang, A.; Jiang, X.; Zhu, J.; Liu, J.; Li, J.; Zhang, G.; Song, C.; Guo, X. Utilization of CO_2 for aromatics production over ZnO/ZrO_2-ZSM-5 tandem catalyst. *J. CO_2 Util.* **2019**, *29*, 140–145. [CrossRef]
2. Science Daily. Available online: https://www.sciencedaily.com/releases/2018/11/181108130533.htm (accessed on 15 June 2023).
3. Ma, Z.; Porosoff, M. Development of tandem catalysts for CO_2 hydrogenation to olefins. *ACS Catal.* **2019**, *9*, 2639–2656. [CrossRef]

4. Li, W.; Zhang, G.; Jiang, X.; Liu, Y.; Zhu, J.; Ding, F.; Liu, Z.; Guo, X.; Song, C. CO_2 hydrogenation on un-promoted and M-promoted Co/TiO_2 catalysts (M = Zr, K, Cs): Effects of crystal phase of supports and metal–support interaction on tuning product distribution. *ACS Catal.* **2019**, *9*, 2739–2751. [CrossRef]
5. Wang, D.; Xie, Z.; Porosoff, M.D.; Chen, J. Recent advances in carbon dioxide hydrogenation to produce olefins and aromatics. *Chem* **2021**, *7*, 2277–2311. [CrossRef]
6. Wei, J.; Yao, R.W.; Ge, Q.J.; Wen, Z.Y.; Ji, X.W.; Fang, C.Y.; Zhang, J.X.; Xu, H.Y.; Sun, J. Catalytic hydrogenation of CO_2 to isoparaffins over Fe-based multifunctional catalysts. *ACS Catal.* **2018**, *8*, 9958–9967. [CrossRef]
7. Wei, J.; Ge, Q.; Yao, R.; Wen, Z.; Fang, C.; Guo, L.; Xu, H.; Sun, J. Directly converting CO_2 into a gasoline fuel. *Nat. Commun.* **2018**, *8*, 15174. [CrossRef]
8. Li, Z.; Wang, J.; Qu, Y.; Liu, H.; Tang, C.; Miao, S.; Feng, Z.; An, H.; Li, C. Highly selective conversion of carbon dioxide to lower olefins. *ACS Catal.* **2017**, *7*, 8544–8548. [CrossRef]
9. Li, Z.L.; Qu, Y.Z.; Wang, J.J.; Liu, H.L.; Li, M.R.; Miao, S.; Li, C. Highly selective conversion of carbon dioxide to aromatics over tandem catalysts. *Joule* **2019**, *3*, 570–583. [CrossRef]
10. Liu, J.H.; Zhang, A.F.; Jiang, X.; Liu, M.; Zhu, J.; Song, C.S.; Guo, X.W. Direct transformation of carbon dioxide to value-added hydrocarbons by physical mixtures of Fe_5C_2 and K-modified Al_2O_3. *Ind. Eng. Chem. Res.* **2018**, *57*, 9120–9126. [CrossRef]
11. Xie, C.L.; Chen, C.; Yu, Y.; Su, J.; Li, Y.F.; Somorjai, G.A.; Yang, P.D. Tandem catalysis for CO_2 hydrogenation to C_2–C_4 hydrocarbons. *Nano Lett.* **2017**, *17*, 3798–3802. [CrossRef]
12. Liu, M.; Yi, Y.H.; Wang, L.; Guo, H.C.; Bogaerts, A. Hydrogenation of carbon dioxide to value-added chemicals by heterogeneous catalysis and plasma catalysis. *Catalysts* **2019**, *9*, 275. [CrossRef]
13. Dang, S.S.; Gao, P.; Liu, Z.Y.; Chen, X.Q.; Yang, C.G.; Wang, H.; Zhong, L.S.; Li, S.G.; Sun, Y.H. Role of zirconium in direct CO_2 hydrogenation to lower olefins on oxide/zeolite bifunctional catalysts. *J. Catal.* **2018**, *364*, 382–393. [CrossRef]
14. Cordero-Lanzac, T.; Ramirez, A.; Navajas, A.; Gevers, L.; Brunialti, S.; Gandía, L.M.; Aguayo, A.T.; Sarathy, S.M.; Gascon, J. A techno-economic and life cycle assessment for the production of green methanol from CO_2: Catalyst and process bottlenecks. *J. Energy Chem.* **2022**, *68*, 255–266. [CrossRef]
15. Ateka, A.; Rodriguez-Vega, P.; Ereña, J.; Aguayo, A.T.; Bilbao, J. Kinetic modeling and reactor design of the direct synthesis of dimethyl ether for CO2 valorization. A review. *Fuel* **2022**, *327*, 125148. [CrossRef]
16. Ateka, A.; Rodriguez-Vega, P.; Ereña, J.; Aguayo, A.T.; Bilbao, J. A review on the valorization of CO_2. Focusing on the thermodynamics and catalyst design studies of the direct synthesis of dimethyl ether. *Fuel Process Technol.* **2022**, *233*, 107310. [CrossRef]
17. Gao, P.; Dang, S.S.; Li, S.G.; Bu, X.N.; Liu, Z.Y.; Qiu, M.H.; Yang, C.G.; Wang, H.; Zhong, L.S.; Han, Y.; et al. Direct production of lower olefins from CO_2 conversion via bifunctional catalysis. *ACS Catal.* **2018**, *8*, 571–578. [CrossRef]
18. Saeidi, S.; Najari, S.; Hessel, V.; Wilson, K.; Keil, F.J.; Concepción, P.; Suib, S.L.; Rodrigues, A.E. Recent advances in CO_2 hydrogenation to value-added products-Current challenges and future directions. *Prog. Energy Combust. Sci.* **2021**, *85*, 100905. [CrossRef]
19. Gnanamani, M.K.; Jacobs, G.; Hamdeh, H.H.; Shafer, W.D.; Liu, F.; Hopps, S.D.; Thomas, G.A.; Davis, B.H. Hydrogenation of carbon dioxide over Co–Fe bimetallic catalysts. *ACS Catal.* **2016**, *6*, 913–927. [CrossRef]
20. Zhang, C.; Xue, Y.; Zheng, X.C.; Qi, L.; Li, Y.L. Loaded Cu-Er metal iso-atoms on graphdiyne for artificial photosynthesis. *Mater. Today* **2023**, *66*, 72–83. [CrossRef]
21. Zheng, Z.Q.; Qi, L.; Gao, Y.Q.; Luan, X.Y.; Xue, Y.R.; He, F.; Li, Y.L. Ir0/graphdiyne atomic interface for selective epoxidation. *Natl. Sci. Rev.* **2023**, *10*, nwad156. [CrossRef]
22. Cui, T.; Dong, J.H.; Pan, X.L.; Yu, T.; Fu, Q.; Bao, X.H. Enhanced hydrogen evolution reaction over molybdenum carbide nanoparticles confined inside single-walled carbon nanotubes. *J. Energy Chem.* **2019**, *28*, 123–127. [CrossRef]
23. Xiao, J.P.; Pan, X.L.; Guo, S.J.; Ren, P.J.; Bao, X.H. Toward Fundamentals of Confined Catalysis in Carbon Nanotubes. *J. Am. Chem. Soc.* **2015**, *137*, 477–482. [CrossRef] [PubMed]
24. Gu, J.; Zhang, Z.Y.; Hu, P.; Xue, N.H.; Peng, L.M.; Guo, X.F.; Lin, M.; Ding, W.P. Platinum Nanoparticles Encapsulated in MFI Zeolite Crystals by a Two-Step Dry Gel Conversion Method as a Highly Selective Hydrogenation Catalyst. *ACS Catal.* **2015**, *5*, 6893–6901. [CrossRef]
25. Yang, G.H.; Kawata, H.; Lin, Q.H.; Wang, J.Y.; Jin, Y.Z.; Zeng, C.Y.; Yoneyama, Y.; Tsubaki, N. Oriented synthesis of target products in liquid-phase tandem reaction over a tripartite zeolite capsule catalyst. *Chem. Sci.* **2013**, *4*, 3958. [CrossRef]
26. Jiang, K.; Siahrostami, S.; Zheng, T.T.; Hu, Y.F.; Hwang, S.; Stavitski, E.; Peng, Y.; Dynes, J.; Gangisetty, M.; Su, D.; et al. Isolated Ni single atoms in graphene nanosheets for high-performance CO_2 reduction. *Energy Environ. Sci.* **2018**, *11*, 893. [CrossRef]
27. Zhan, G.; Zeng, H.C. ZIF-67-derived nanoreactors for controlling product selectivity in CO_2 hydrogenation. *ACS Catal.* **2017**, *7*, 7509–7519. [CrossRef]
28. Li, S.W.; Tuel, A.; Meunier, F.; Aouine, M.; Farrusseng, D. Platinum nanoparticles entrapped in zeolite nanoshells as active and sintering-resistant arene hydrogenation catalysts. *J. Catal.* **2015**, *332*, 25–30. [CrossRef]
29. Wang, T.S.; Gao, L.J.; Hou, J.W.; Herou, S.J.A.; Griffiths, J.T.; Li, W.W.; Dong, J.H.; Gao, S.; Titirici, M.; Kumar, R.V.; et al. Rational approach to guest confinement inside MOF cavities for low-temperature catalysis. *Nat. Commun.* **2019**, *10*, 1340. [CrossRef]
30. Goel, S.; Wu, Z.J.; Zones, I.; Iglesia, S.I.; Iglesia, E. Synthesis and Catalytic Properties of Metal Clusters Encapsulated within Small-Pore ((SOD, GIS, ANA) Zeolites. *J. Am. Chem. Soc.* **2012**, *134*, 17688–17695. [CrossRef]

31. Wang, X.F.; Cui, Y.Z.; Wang, Y.; Song, X.W.; Yu, J.H. Fabrication and Catalytic Performance of Highly Stable Multifunc-tional Core–Shell Zeolite Composites. *Inorg. Chem.* **2013**, *52*, 10708–10710. [CrossRef]
32. He, J.J.; Liu, Z.L.; Yoneyama, Y.; Nishiyama, N.; Tsubaki, N. Multiple-Functional Capsule Catalysts: A Tailor-Made Confined Reaction Environment for the Direct Synthesis of Middle Isoparaffins from Syngas. *Chem. Eur. J.* **2006**, *12*, 8296–8304. [CrossRef]
33. Farrusseng, D.; Tuel, A. Perspectives on zeolite-encapsulated metal nanoparticles and their applications in catalysis. *New J. Chem.* **2016**, *40*, 3933–3949. [CrossRef]
34. Ren, N.; Yang, Y.H.; Shen, J.; Zhang, Y.H.; Xu, H.L.; Gao, Z.; Tang, Y. Novel, efficient hollow zeolitically microcapsulized noble metal catalysts. *J. Catal.* **2007**, *251*, 182–188. [CrossRef]
35. Weber, D.; He, T.; Wong, M.; Moon, C.; Zhang, A.; Foley, N.; Ramer, N.J.; Zhang, C. Recent Advances in Mitigating Catalyst Deactivation of CO_2 Hydrogenation to Light Olefins. *Catalysts* **2021**, *11*, 1447. [CrossRef]
36. Zhang, C.; Bhargava, G.; Elwell, M.D.; Parasher, S.; Zhou, B.; Yates, D.; Knoke, I.; Neitzel, I.; Gogotsi, Y. Hollow graphitic carbon nanospheres: Synthesis and properties. *J. Mater. Sci.* **2014**, *49*, 1947–1956. [CrossRef]
37. Xiang, W.L.; Zhang, Y.P.; Lin, H.F.; Liu, C.J. Nanoparticle/metal–organic framework composites for catalytic applications: Current status and perspective. *Molecules* **2017**, *22*, 2103. [CrossRef]
38. Li, W.H.; Wang, H.Z.; Jiang, X.; Zhu, J.; Liu, Z.M.; Guo, X.W.; Song, C.S. A short review of recent advances in CO_2 hydrogenation to hydrocarbons over heterogeneous catalysts. *RSC Adv.* **2018**, *8*, 7651. [CrossRef]
39. Yan, Q.G.; Li, J.H.; Zhang, X.F.; Zhang, J.L.; Cai, Z.Y. Mass production of graphene materials from solid carbon sources using a molecular cracking and welding method. *J. Mater. Chem. A* **2019**, *7*, 13978–13985. [CrossRef]
40. Gupta, S.; Jain, V.K.; Jagadeesan, D. Fine tuning the composition and nanostructure of Fe-based core–shell nanocatalyst for efficient CO2 hydrogenation. *ChemNanoMat* **2016**, *2*, 989–996. [CrossRef]
41. Han, Y.Q.; Xu, H.T.; Su, Y.Q.; Xu, Z.L.; Wang, K.F.; Wang, W.Z. Noble metal (Pt, Au@Pd) nanoparticles supported on metal organic framework (MOF-74) nanoshuttles as high-selectivity CO_2 conversion catalysts. *J. Catal.* **2019**, *370*, 70–78. [CrossRef]
42. Jiang, Q.; Lan, D.P.; Zhao, G.F.; Xu, H.T.; Gong, X.D.; Liu, J.C.; Shi, Y.; Zhang, L.D.; Fang, H.M.; Cheng, D.H.; et al. Converting CO_2 Hydrogenation Products from Paraffins to Olefins: Modification of Zeolite surface properties by a UIO-n membrane. *ACS Catal.* **2022**, *12*, 5894–5902. [CrossRef]
43. Tu, J.L.; Ding, M.Y.; Zhang, Q.; Zhang, Y.L.; Wang, C.G.; Wang, T.J.; Ma, L.L.; Li, X.J. Design of carbon-encapsulated Fe_3O_4 nanocatalyst with enhanced performance for Fischer–Tropsch synthesis. *ChemCatChem* **2015**, *7*, 2323–2327. [CrossRef]
44. Chen, W.; Fan, Z.; Pan, X.; Bao, X.; Chen, W.; Fan, Z.; Pan, X.; Bao, X. Effect of Confinement in carbon nanotubes on the activity of Fischer–Tropsch iron catalyst. *J. Am. Chem. Soc.* **2008**, *130*, 9414–9419. [CrossRef] [PubMed]
45. Chen, H.; Liu, J.; Liu, P.; Wang, Y.; Xiao, H.; Yang, Q.; Feng, X.; Zhou, S. Carbon-confined magnesium hydride nano-lamellae for catalytic hydrogenation of carbon dioxide to lower olefins. *J. Catal.* **2019**, *379*, 121–128. [CrossRef]
46. Sánchez-Contador, M.; Ateka, A.; Aguayo, A.T.; Bilbao, J. Direct synthesis of dimethyl ether from CO and CO_2 over a core-shell structured CuO-ZnO-ZrO_2@SAPO-11 catalyst. *Fuel Process. Technol.* **2018**, *179*, 258–268. [CrossRef]
47. Ateka, A.; Sánchez-Contador, M.; Portillo, A.; Bilbao, J.; Aguayo, A.T. Kinetic modeling of CO_2+CO hydrogenation to DME over a CuO-ZnO-ZrO2@SAPO-11 core-shell catalyst. *Fuel Process Technol.* **2020**, *206*, 106434. [CrossRef]
48. Wu, T.; Lin, J.; Cheng, Y.; Tian, J.; Wang, S.; Xie, S.; Pei, Y.; Yan, S.; Qiao, M.; Xu, H.; et al. Porous graphene-conned Fe–K as highly ecient catalyst for CO_2 direct hydrogenation to light olens. *ACS Appl. Mater. Interfaces* **2018**, *10*, 23439–23443. [CrossRef]
49. Wei, J.; Sun, J.; Wen, Z.; Fang, C.; Ge, Q.; Xu, H. New insights into the effect of sodium on Fe_3O_4-based nanocatalysts for CO_2 hydrogenation to light olefins. *Catal. Sci. Technol.* **2016**, *6*, 4786–4793. [CrossRef]
50. Wezendonk, T.A.; Sun, X.; Dugulan, A.I.; van Hoof, A.J.F.; Hensen, E.J.M.; Kapteijn, F.; Gascon, J. Controlled formation of iron carbides and their performance in Fischer-Tropsch synthesis. *J. Catal.* **2018**, *362*, 106–117. [CrossRef]
51. Weber, D.; Rui, N.; Zhang, F.; Zhang, H.; Vovchok, D.; Wildy, M.; Arizapana, K.; Saporita, A.; Zhang, J.Z.; Senanayake, S.D.; et al. Carbon Nanosphere-Encapsulated Fe Core–Shell Structures for Catalytic CO_2 Hydrogenation. *ACS Appl. Nano Mater.* **2022**, *5*, 11605–11616. [CrossRef]
52. Weber, D.; Zhang, H.; Gandotra, A.; Schossig, J.; Rui, N.; Wildy, M.; Wei, W.Y.; Arizapana, K.; Forte, N.; Zhang, J.Z.; et al. CO_2 conversion to value-added chemicals over carbon nano-sphere encapsulated Fe-Co catalysts. *ACS Appl. Mater. Interfaces* **2023**. *submitted*.
53. Xu, Q.; Xu, X.; Fan, G.; Yang, L.; Li, F. Unveiling the roles of Fe-Co interactions over ternary spinel-type $ZnCo_xFe_{2-x}O_4$ catalysts for highly efficient CO_2 hydrogenation to produce light olefins. *J. Catal.* **2021**, *400*, 355–366. [CrossRef]
54. Yuan, F.; Zhang, G.; Zhu, J.; Ding, F.; Zhang, A.; Song, C.; Guo, X. Boosting light olefin selectivity in CO_2 hydrogenation by adding Co to Fe catalysts within close proximity. *Catal. Today* **2021**, *371*, 142–149. [CrossRef]
55. Wei, C.; Tu, W.; Jia, L.; Liu, Y.; Lian, H.; Wang, P.; Zhang, Z. The evolutions of carbon and iron species modified by Na and their tuning effect on the hydrogenation of CO_2 to olefins. *Appl. Surf. Sci.* **2020**, *525*, 146622. [CrossRef]
56. Yang, S.; Chun, H.; Lee, S.; Han, S.J.; Lee, K.; Kim, Y.T. Comparative study of olefin production from CO and CO_2 Using Na-and K-promoted zinc ferrite. *ACS Catal.* **2020**, *10*, 10742–10759. [CrossRef]
57. Liang, B.; Duan, H.; Sun, T.; Ma, T.; Liu, X.; Xu, J.; Su, X.; Huang, Y.; Zhang, T. Effect of Na promoter on Fe-based catalyst for CO_2 hydrogenation to alkenes. *ACS Sustain. Chem. Eng.* **2019**, *7*, 925–932. [CrossRef]
58. Ramirez, A.; Gevers, L.; Bavykina, A.; Ould-Chikh, S.; Gascon, J. Metal organic framework-derived iron catalysts for the direct hydrogenation of CO_2 to short chain olefins. *ACS Catal.* **2018**, *8*, 9174–9182. [CrossRef]

59. Numpilai, T.; Chanlek, N.; Poo-Arporn, Y.; Cheng, C.K.; Siri-Nguan, N.; Sornchamni, T.; Chareonpanich, M.; Kongkachuichay, P.; Yigit, N.; Rupprechter, G.; et al. Tuning interactions of surface-adsorbed species over Fe-Co/K-Al_2O_3 catalyst by different K content: Selective CO_2 hydrogenation to light olefins. *ChemCatChem* **2020**, *12*, 3306–3320. [CrossRef]
60. Boreriboon, N.; Jiang, X.; Song, C.; Prasassarakich, P. Fe-based bimetallic catalysts supported on TiO_2 for selective CO_2 hydrogenation to hydrocarbons. *J. CO2 Util.* **2018**, *25*, 330–337. [CrossRef]
61. Jiang, J.; Wen, C.; Tian, Z.; Wang, Y.; Zhai, Y.; Chen, L.; Li, Y.; Liu, Q.; Wang, C.; Ma, L. Manganese-promoted Fe_3O_4 microsphere for efficient conversion of CO_2 to light olefins. *Ind. Eng. Chem. Res.* **2020**, *59*, 2155–2162. [CrossRef]
62. Liang, B.; Sun, T.; Ma, J.; Duan, H.; Li, L.; Yang, X.; Zhang, Y.; Su, X.; Huang, Y.; Zhang, T. Mn decorated Na/Fe catalysts for CO_2 hydrogenation to light olefins. *Catal. Sci. Technol.* **2019**, *9*, 456–464. [CrossRef]
63. Zhang, J.; Su, X.; Wang, X.; Ma, Q.; Fan, S.; Zhao, T. Promotion effects of Ce added Fe–Zr–K on CO_2 hydrogenation to light olefins. *React. Kinet. Mech. Catal.* **2018**, *124*, 575–585. [CrossRef]
64. Chaipraditgul, N.; Numpilai, T.; Cheng, C.K.; Siri-Nguan, N.; Sornchamni, T.; Wattanakit, C.; Limtrakul, J.; Witoon, T. Tuning interaction of surface-adsorbed species over Fe/K-Al_2O_3 modified with transition metals (Cu, Mn, V, Zn or Co) on light olefins production from CO_2 hydrogenation. *Fuel* **2021**, *283*, 119248. [CrossRef]
65. Gnanamani, M.K.; Jacobs, G.; Hamdeh, H.H.; Shafer, W.D.; Liu, F.; Hopps, S.D.; Thomas, G.A.; Davis, B.H. Hydrogenation of carbon dioxide over iron carbide prepared from alkali metal promoted iron oxalate. *Appl. Catal. A Gen.* **2018**, *564*, 243–249. [CrossRef]
66. Guo, L.; Sun, J.; Ji, X.; Wei, J.; Wen, Z.; Yao, R.; Xu, H.; Ge, Q. Directly converting carbon dioxide to linear α-olefins on bio-promoted catalysts. *Commun. Chem.* **2018**, *1*, 11. [CrossRef]
67. Witoon, T.; Chaipraditgul, N.; Numpilai, T.; Lapkeatseree, V.; Ayodele, B.; Cheng, C.; Siri-Nguan, N.; Sorn-chamni, T.; Limtrakul, J. Highly active Fe-Co-Zn/K-Al_2O_3 catalysts for CO_2 hydrogenation to light olefins. *Chem. Eng. Sci.* **2021**, *233*, 116428. [CrossRef]
68. Li, Z.Q.; Lu, C.J.; Xia, Z.P.; Zhou, Y.; Luo, Z. X-ray diffraction patterns of graphite and turbostratic carbon. *Carbon* **2007**, *45*, 1686–1695. [CrossRef]
69. Wang, H.; Zhou, W.; Ho, D.L.; Winey, K.I.; Fischer, J.E.; Glinka, C.J.; Hobbie, E.K. Dispersing single-walled carbon nanotubes with surfactants: A small angle neutron scattering study. *Nano. Lett.* **2004**, *4*, 1789–1793. [CrossRef]
70. Vix-Guterl, C.; Couzi, M.; Dentzer, J.; Trinquecoste, M.; Delhaes, P. Surface Characterizations of Carbon Multiwall Nanotubes: Comparison between Surface Active Sites and Raman Spectroscopy. *J. Phys. Chem. B* **2004**, *108*, 19361–19367. [CrossRef]
71. Zhang, C.; Cao, C.; Zhang, Y.; Liu, X.; Xu, J.; Zhu, M.; Tu, W.; Han, Y. Unraveling the role of zinc on bimetallic Fe_5C_2–ZnO catalysts for highly selective carbon dioxide hydrogenation to high carbon α-olefins. *ACS Catal.* **2021**, *11*, 2121–2133. [CrossRef]
72. Zhou, B.; Zhang, C.; Balee, R. Polymeric Materials Incorporating Carbon Nanosphere Nanostructures. U.S. Patent 7935276B2, 9 December 2010.
73. Zhang, C.; Fransson, M.; Liu, C.K.; Zhou, B. Carbon Nanostructures Manufactured from Catalytic Templating Nanoparticles. U.S. Patent 7718155B2, 18 May 2010.
74. Zhang, C.; Gao, Q.H.; Parasher, S.; Yates, D. d-Glucose mitigates the agglomeration of the hollow graphitic carbon nano-spheres. *J. Mater. Sci.* **2017**, *52*, 5968–5980. [CrossRef]
75. Zhang, C.; Gao, Q.S.; Zhou, B.; Bhargava, G. Preparation, characterization, and surface conductivity of nanocomposites with hollow graphitic carbon nanosphere as fillers in polymethylmethacry-late matrix. *J. Nanopart. Res.* **2017**, *19*, 269. [CrossRef]